

## Near-Inertial Waves on the New England Shelf: The Role of Evolving Stratification, Turbulent Dissipation, and Bottom Drag

J. A. MACKINNON

*Scripps Institution of Oceanography, University of California, San Diego, La Jolla, California*

M. C. GREGG

*Applied Physics Laboratory, and School of Oceanography, University of Washington, Seattle, Washington*

(Manuscript received 16 June 2004, in final form 12 May 2005)

### ABSTRACT

Energetic variable near-inertial internal waves were observed on the springtime New England shelf as part of the Coastal Mixing and Optics (CMO) project. Surface warming and freshwater advection tripled the average stratification during a 3-week observational period in April/May 1997. The wave field was dominated by near-inertial internal waves generated by passing storms. Wave evolution was controlled by a balance among wind stress, bottom drag, and turbulent dissipation. As the stratification evolved, the vertical structure of these near-inertial waves switched from mode 1 to mode 2 with associated changes in the magnitude and location of wave shear. The growth of mode-2 waves was attributable to a combination of changing wind stress forcing and a nonlinear coupling between the first and second vertical modes through quadratic bottom stress. To explore both forcing mechanisms, an open-ocean mixed layer model is adapted to the continental shelf. In this model, surface wind stress and bottom stress are distributed over the surface and bottom mixed layers and then projected onto orthogonal vertical modes. The model replicates the correct magnitude and evolving modal distribution of the internal waves and confirms that bottom stress can act to transfer energy between internal wave modes.

### 1. Introduction

Near-inertial wave generation has been well studied in the open ocean, from Pollard and Millard (1970) to the comprehensive Ocean Storms Experiment (see D'Asaro 1995 for an overview) to recent work by Alford (2001). Mixed layer motions are well modeled by simple slab-layer models of wind input (Pollard and Millard 1970; D'Asaro 1985). Vertically propagating internal waves are subsequently generated by horizontal convergences of mixed layer motions (D'Asaro et al. 1995; Young and Ben-Jelloul 1997; Moehlis and Llewellyn-Smith 2001).

On continental shelves, internal waves are an integral link in the pathway between external energy sources (wind, tides, solar heating) and turbulent dissipation. As such, understanding the generation, evolution, and

eventual decay of coastal internal waves is important both for closing the oceanic energy budget and for diagnosing local mixing rates of heat, salt, and nutrients. The fate of internal waves on the shelf depends on an interplay among internal wave shear ( $S$ ), stratification ( $N$ ), and turbulent dissipation ( $\epsilon$ ). Turbulent energy dissipation may be diagnosed or modeled as a function of stratification and the local shear field, which is in general a complicated function of the time-varying energy and vertical structure of the waves present (MacKinnon and Gregg 2003a, 2005; Polzin et al. 1995; Gregg 1989). Turbulence can in turn drain energy from internal waves.

Most studies of internal waves on continental shelves have focused on internal tides (Rippeth and Inall 2002; Holloway et al. 2001) and associated nonlinear internal solitons (Sandstrom et al. 1989; Apel et al. 1995; Colosi et al. 2001; MacKinnon and Gregg 2003b). Relatively few studies have looked at wind-generated, near-inertial waves on shelves. Chant (2001) and Chen et al. (1996) report observations of low-mode near-inertial internal waves that are consistent with local wind forc-

---

*Corresponding author address:* Jennifer MacKinnon, SIO/UCSD, 9500 Gilman Drive, Mail Code 0213, La Jolla, CA 92093-0213.

E-mail: jen@coast.ucsd.edu

ing. Van Haren et al. (1999) examine near-inertial waves in the North Sea that experience complicated feedbacks with evolving stratification and a strong seasonal cycle. Shearman (2005) conducts a careful study of annual variability in near-inertial currents on the New England shelf. He generally observes a mode-1 baroclinic structure that is coherent across nearly the entire shelf, with a magnitude that decreases onshore.

The Coastal Mixing and Optics (CMO) project provided an opportunity to integrate measurements of wave shear, stratification, and turbulent dissipation. Two previous papers (MacKinnon and Gregg 2003b, hereinafter MGb; MacKinnon and Gregg 2003a, hereinafter MGa) discussed the internal wave field and associated turbulent dissipation during late summer 1996. The internal wave field was dominated by near-inertial and semidiurnal waves, and episodic solitons. Wave energy was largely concentrated in low modes and, to the extent that higher-mode waves were observed, they were uncorrelated with lower modes. Turbulent dissipation was related to shear from local internal waves, though the nature of that relationship was different between solitons and other waves and did not agree with commonly used turbulence parameterizations derived for the open ocean thermocline.

The spring 1997 portion of the CMO project took place during the spring stratification period (Gardner et al. 2001; Lentz et al. 2003). This timing permitted observations of wave generation, evolution, and decay through a variety of stratification regimes. This paper focuses on the generation, evolution, and decay of near-inertial internal waves. The absence of an internal tide during this time allows us to consider one-dimensional models of near-inertial wave generation and decay. In a companion paper (MacKinnon and Gregg 2005, hereinafter MG05), we describe patterns of observed turbulence, consider several dynamic and kinematic models of turbulence production, and discuss the effect of turbulent mixing on the evolving stratification.

The outline of this paper is as follows: in section 2 we describe the experiment and instrumentation used; observations of the magnitude and evolving vertical structure of near-inertial waves are presented in section 3, preceded by a discussion of relevant background water properties and meteorological forcing; sections 4 and 5 analyze the energetics and vertical structure of observed waves in terms of surface forcing, bottom drag, and interior dissipation using baroclinic mode decompositions; in section 6, we embody the hypotheses of previous sections in a simple numerical model that extends the slab models used in the open ocean to include discrete baroclinic modes and realistic bottom drag; and conclusions are presented in section 7.

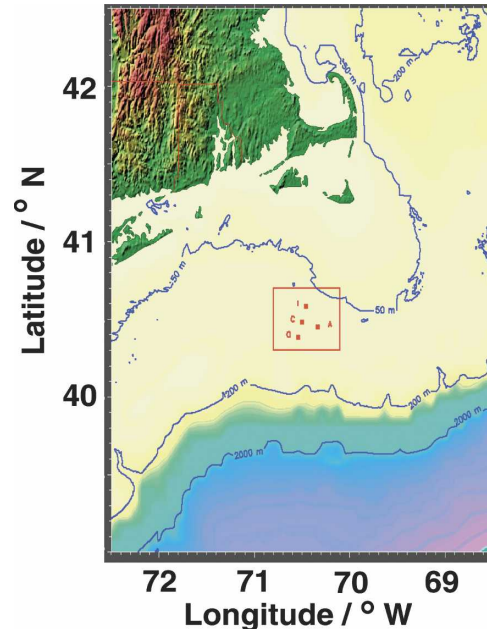


FIG. 1. Location of the CMO experiment. Profiling took place near the central site (labeled “C”), in a 1.5-km-wide box (not shown).

## 2. Experimental methods

### a. Experiment

A series of microstructure measurements were made on board the R/V *Knorr* as part of the Coastal Mixing and Optics Experiment. From 26 April to 12 May 1997, we obtained microstructure, acoustic Doppler current profiler (ADCP), and echosounder data in the region known as the “mud patch” near the 70-m isobath south of Nantucket (Fig. 1). We were forced to return to shore for a medical emergency from 2 to 4 May, resulting in a gap in the data. The vessel steamed slowly east and west (to prevent the profiler from moving under the ship) in a box 1.5 km alongshelf and 1 km across shelf centered near 40°30'N, 70°30'W. Our date convention is that local noon 1 January is yearday 0.5.

### b. Meteorological measurements

Meteorological data presented are primarily from the improved meteorological (IMET) sensor on board the *Knorr*. During our absence from the site on yeardays 121–123, we supplement these data with measurements from the Woods Hole Oceanographic Institution meteorological mooring located nearby (courtesy of S. Anderson, S. Lentz, and A. Plueddemann, WHOI). While we were on station, the two records were nearly identical. Surface wind stress ( $\tau_s$ ) was calculated from

the measured IMET quantities using the stability method described in Fairall et al. (1996).

### c. Velocity

We obtained continuous time series of velocity at 1-min intervals and 4-m vertical spacing between 12 and 52 m from a 150-kHz broadband shipboard ADCP. Data during yearday 121 were unreliable owing to instrument noise. During this day, and our subsequent 2-day absence, the data presented here have been supplemented with velocity from an upward-looking RD Instruments ADCP on a nearby (0.75 km) mooring (courtesy of T. Dickey, University of California, Santa Barbara). Internal ADCP bin averaging is equivalent to applying an 8-m Bartlett filter to all velocity data; hence only every other depth bin is truly independent. To carry out full water column integrations, we assume that velocity above (below) the shallowest (deepest) measured values within the surface (bottom) mixed layer is constant.

Baroclinic velocity was computed by removing the depth mean of each velocity component. Shear variance ( $S^2$ ) was calculated by first differencing and squaring composite velocity over 4-m intervals. There is a loss in shear variance due to both first differencing and the Bartlett filter. Though specific phase information of the lost shear cannot be regained, we estimated that average 4-m shear variance would be 1.5 times the variance measured based on spectra of observed shear and knowledge of the filter transfer functions. None of the variance loss estimates were used to correct the data.

### d. Hydrography

Density measurements presented here were made by the Modular Microstructure Profiler (MMP), a loosely tethered free-falling instrument that was ballasted to fall at a rate of  $50 \text{ cm s}^{-1}$ . A complete water column profile took approximately four minutes during peak operating efficiency, resulting in 2195 total profiles. The MMP is equipped with SeaBird temperature and conductivity sensors, from which density is calculated. Shipboard scheduling required our profiling to primarily take place at night. During daytime, density data were supplemented with shipboard CTD data, courtesy of W. Gardner (Texas A&M University). Owing to a higher noise level in CTD density measurements, full CTD-derived buoyancy frequencies are not included in Fig. 2, though a smoothed version is used to calculate mode shapes (section 3d). Though MMP and CTD quantities are measured as a function of pressure, here all quantities are plotted versus depth for comparison with ADCP data, which produces an average error of less than 1%. Depth is defined to be positive upward.

## 3. Basic observations

In this section, we present an overview of the observed wave magnitude and vertical structure as well as a description of the meteorological conditions (wind stress), water properties (stratification), and turbulent energy dissipation, which we will directly relate to wave generation and evolution in subsequent sections. A more detailed discussion of the evolving water properties in light of surface fluxes and turbulent redistribution of heat and salt is presented in MG05.

### a. Wind forcing

Wind stress ranged over an order of magnitude as storms passed every few days (Fig. 2). The strongest winds occurred during a storm on yeardays 117–118, with wind stress rising above  $0.4 \text{ N m}^{-2}$ . A second period of strong winds occurred on yeardays 121–123, during our absence from the site. A weaker but more sustained period of elevated wind stress began on yearday 125 and lasted for several days.

### b. Stratification

Stratification tripled and underwent significant changes in vertical structure over the fortnight of observations (Fig. 2). We define the surface (bottom) mixed layer as that region with density within  $0.01 \text{ kg m}^{-3}$  of the smallest (largest) measured density for a given profile. Average surface and bottom mixed layer heights were 14 and 25 m, both significantly larger than those observed in the late summer (MGa). Density evolution was controlled by surface heating, mixed layer entrainment during periods of strong wind stress, and advection of near-surface freshwater (Lentz et al. 2003; MG05). Density initially displayed a two-layer structure, which was particularly sharp after the mixing associated with each passing storm (yeardays 118, 123). By yearday 126, density gradients were stronger overall and more continuous, with some concentration below the surface mixed layer and above the bottom mixed layer.

### c. Internal waves: Magnitude

Low-mode clockwise-rotating internal waves arose after the passage of each storm (Fig. 2). During the storm on yearday 117, strong internal waves appeared, visible both in baroclinic velocity (Fig. 2) and depth-integrated baroclinic energy (Fig. 4). These waves mostly disappeared after a single inertial period ( $2\pi/f = 18.7 \text{ h}$ ). Further waves appeared after the pair of wind bursts on yeardays 121–123, and again decayed in approximately one inertial period. During

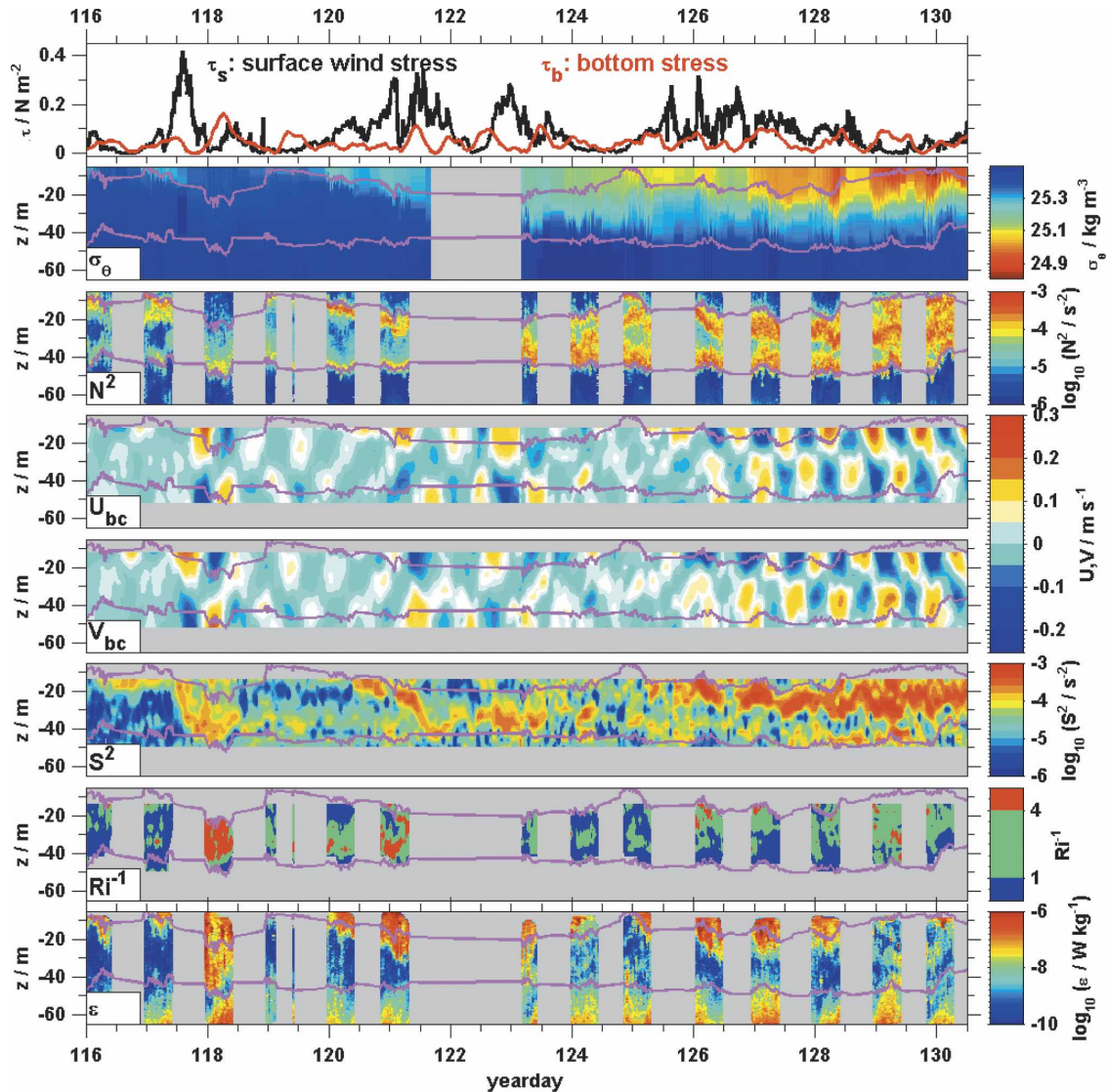


FIG. 2. (top to bottom) Wind stress and bottom stress, potential density, buoyancy frequency, baroclinic eastward and northward velocity, shear variance, inverse Richardson number, and turbulent dissipation rate. The magenta lines indicate the surface and bottom mixed layer edges, as defined by a 0.01  $\sigma_\theta$  criterion. Density data have been supplemented with *Knorr* CTD data (courtesy of W. Gardner). Velocity and shear data have been supplemented with University of California, Santa Barbara, (UCSB) mooring data (courtesy of T. Dickey).

the lower, but more sustained, wind stress starting on yearday 125, internal waves appeared and persisted through the end of the record, even after the wind stress declined. A spectral analysis shows baroclinic energy to have been primarily near inertial, with a peak at 1.05*f* (Fig. 3). Unlike the summertime observations reported in MGb, there was no sign of an internal tide in the spring.

Internal waves were superimposed on a strong barotropic tide and weaker subtidal barotropic flow (Figs. 3 and 4). Baroclinic energy was on average 30% of the

barotropic energy ( $6.4 \times 10^{-3} \text{ J kg}^{-1}$  versus  $22 \times 10^{-3} \text{ J kg}^{-1}$ ), though it exceeded barotropic energy when strong internal waves were present (Fig. 4b).

#### d. Internal waves: Vertical structure

Internal waves evolved from a dominantly first-mode structure to include substantial second- and third-mode components. The waves generated after the passage of the first two storms (yeardays 118 and 121–123) were primarily mode 1, with flow above 30–40 m opposing deeper currents (Figs. 2, 5). The waves that arose after

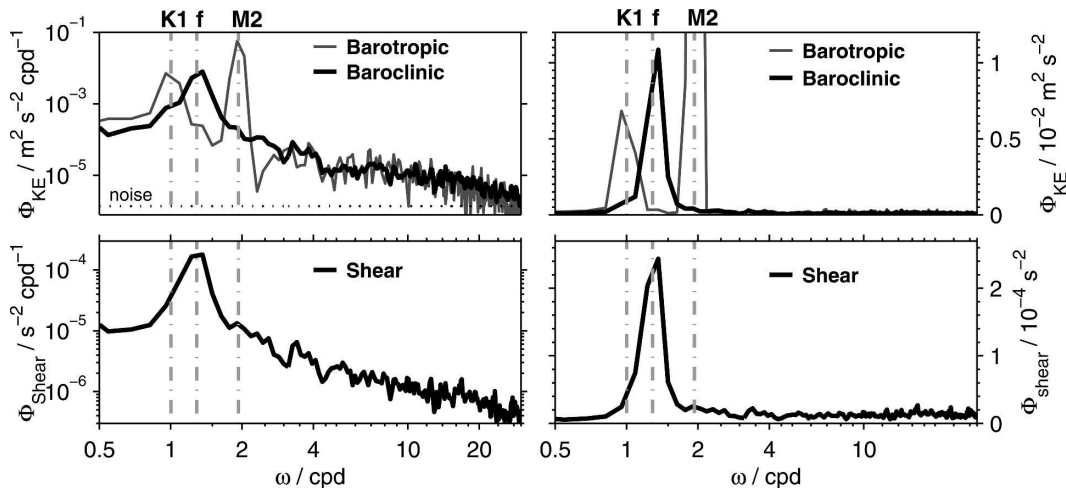


FIG. 3. (top left) Depth-averaged energy spectra for barotropic and baroclinic energy with diurnal, inertial, and semidiurnal frequencies indicated. The horizontal dotted line indicates a spectral noise level based on a velocity uncertainty of  $0.01 \text{ m s}^{-1}$ . (bottom left) Depth-averaged spectrum of shear variance, and (right) variance preserving. All spectra are based on shipboard velocity between yeardays 123 and 130.

yearday 126 had a higher-mode structure, with peaks in velocity in the upper 25 m and near 40 m.

Baroclinic velocity can be formally decomposed onto a set of orthogonal vertical modes given by the Taylor–Goldstein equation with no mean shear. The vertical structure of each mode is governed by (Gill 1982; Thorpe 1998; Levine 2002; MGb)

$$\psi_j''(z) = -\left[\frac{N^2(z)}{c_j^2}\right]\psi_j(z) \quad \text{and} \quad (1)$$

$$\psi_j(-H) = \psi_j(0) = 0, \quad (2)$$

where  $c_j$  is a separation constant (eigenvalue) and waves are assumed to be hydrostatic. Vertical velocity

and vertical displacement associated with each mode are proportional to  $\psi_j$ , while the horizontal velocity is proportional to  $d\psi_j/dz$ .

The shape of each baroclinic mode,  $\psi_j(z)$ , evolved in response to changing stratification. Theoretical mode shapes are calculated based on (1) and a slowly evolving (low passed below 2 cpd) stratification profile. Figure 5 shows the shapes of the first three baroclinic modes early and late in the observational period. Each component of velocity can be written as a sum of modal contributions. For example, eastward velocity is given by

$$u(z, t) = \sum U_j(t) \frac{\partial \psi_j(z, t)}{\partial z}, \quad (3)$$

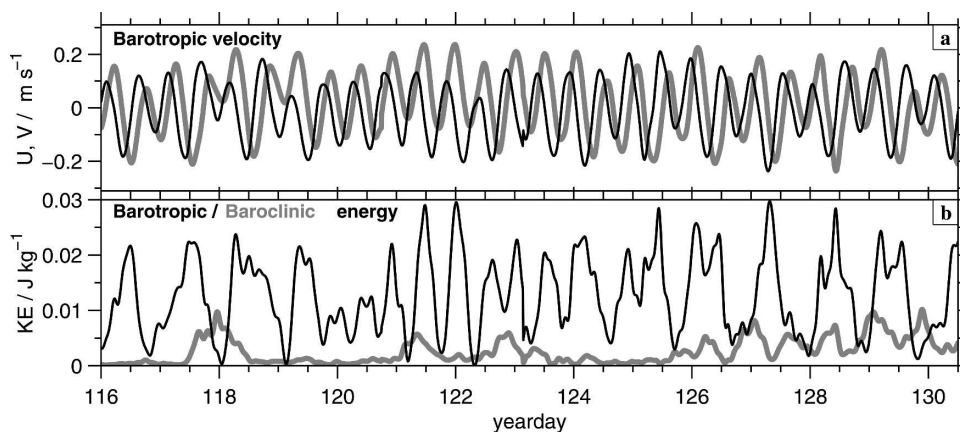


FIG. 4. (a) Barotropic eastward (thick, gray) and northward (thin, black) velocity and (b) depth-integrated barotropic (thin, black) and baroclinic (thick, gray) horizontal kinetic energy. Shipboard ADCP data have been supplemented with UCSB moored velocity measurements.

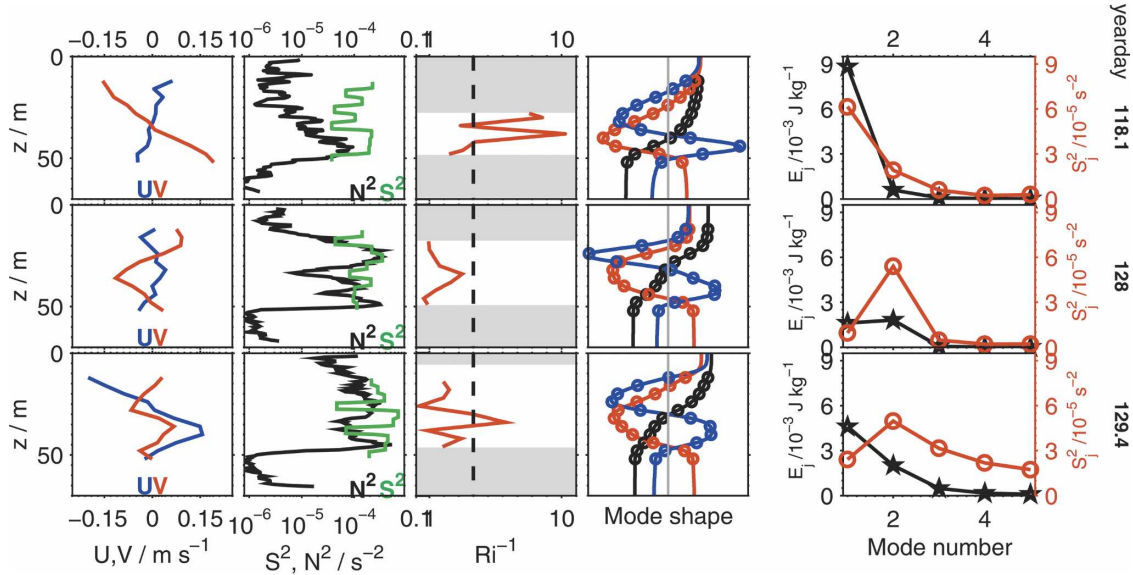


FIG. 5. (top) Average profiles of various quantities averaged over 20 min centered on yearday (top) 118.1, (middle) 128, and (bottom) 129.4: (left to right) baroclinic eastward (blue) and northward (red) velocity, stratification (black) and shear variance (green), inverse 4-m Richardson number, vertical shapes of the first three baroclinic modes for this stratification, with circles indicating the locations of ADCP bins and a gray zero-line for reference, and energy (black, left axis) and shear variance (red, right axis) in the first five baroclinic modes. Shading in the middle panel shows the boundaries of surface and bottom mixed layers.

where  $\psi_j(z, t)$  is assumed to evolve much more slowly in time than  $U_j(t)$ .

The amplitude ( $\text{m s}^{-1}$ ) of each mode can be represented by a vector

$$\mathbf{U}_j = U_j, V_j. \quad (4)$$

Observed velocity is projected onto the barotropic and first four baroclinic modes using a least squares regression at each time. The calculation was extended to the surface and bottom assuming constant velocity above 12 m and below 52 m; both depth ranges were almost always within surface and bottom mixed layers (Fig. 2; MG05).

Calculated modal amplitudes reveal the growing relative importance of second- and third-mode waves, especially as a percentage of shear variance. Figure 6 shows the distribution of energy and shear variance between vertical modes in comparison with total energy and shear. The cruise-averaged sum of baroclinic mode energies ( $2.8 \times 10^{-3} \text{ J kg}^{-1}$ ) agrees well with the total depth-averaged baroclinic energy ( $2.7 \times 10^{-3} \text{ J kg}^{-1}$ ). The first four modes contained 76%, 17%, 5%, and 2% of the average baroclinic energy, respectively. The percentage of energy in the second mode shifted from 12% before yearday 126 to 22% afterward.

There are several sources of uncertainty in our

mode-amplitude calculations. First, while mode shapes are strictly orthogonal over the whole water depth (their products integrate to zero), there is significant overlap in mode shape between 12 and 52 m (Fig. 5). In particular, there is strong overlap in the nondimensional structure of modes 1 and 3 over this depth range. As a result, a least squares regression of a pure mode-1 wave will spuriously project amplitude onto both mode-1 and mode-3 shapes. Similarly, there is overlap between modes 2 and 4 over this depth range. Given the strength of the first two modes, we assume that these projected amplitudes are relatively robust, while the higher-mode amplitudes are more dubious. Extending the shallowest (deepest) observed velocities above (below) the ADCP depth range gives implicit preference to the lowest modes, which have minimal gradients in these depth ranges. In subsequent analysis, we concentrate on the first two modes only. Second, the stratification sometimes changed on a time scale comparable to the inertial period, for example, following the storm on yearday 118 (Fig. 2). During such periods, the modal decomposition technique is questionable.

#### e. Internal waves: Shear variance

Shear variance was sensitive to both the strength and the changing vertical structure of baroclinic energy. During the first two periods of elevated internal wave

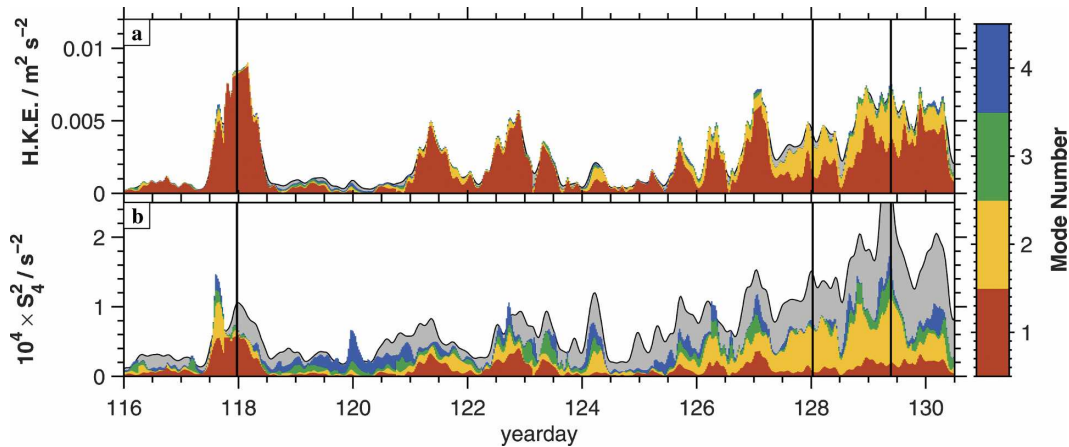


FIG. 6. (a) Stacked histograms of energy variance in the first four baroclinic modes. Depth-averaged baroclinic energy is represented by the gray-shaded area bounded by a (barely visible) black line. (b) Stacked histograms of shear variance from the first four modes. Depth-averaged shear variance shown in gray. UCSB moored velocities have been incorporated during gaps in shipboard ADCP data. The three vertical black lines indicate the times of three sample periods that are shown in Fig. 5.

energy (yeardays 118 and 121–123), shear was concentrated near the zero-crossing of these first-mode waves (Fig. 2). On yearday 118, the strongest shear was at and above the region of peak stratification. After yearday 126, shear was stronger and was at times split into two peak regions: a strong patch that migrated between 15 and 35 m and a smaller maximum below 40 m. Higher modes contribute relatively more to shear variance than to energy; overall, 53% of shear variance is contained within the first four modes (Fig. 6). The dominant contributor to shear variance changed from mode 1 on yearday 118 to mode 2 between yeardays 127 and 129 (Figs. 5, 6).

The inverse gradient Richardson number

$$\text{Ri}^{-1} = \frac{S^2}{N^2} \quad (5)$$

is often linked to dynamic instability and turbulence, either through direct shear instability or wave–wave interaction (Kunze et al. 1990; Polzin 1996; MG05). Theory and experiment have shown that a steady shear flow is stable to shear instability as long as the inverse Richardson number remains below 4 (Miles 1961; Thorpe 1978). The inverse gradient Richardson number was well above the critical value during the moderately strong shear and weak stratification on yeardays 118 and 121. It was lower than, but still close to, the threshold after yearday 126 when both shear and stratification were stronger (Figs. 2, 5).

#### f. Dissipation

Turbulent energy dissipation ranged over four orders of magnitude and was concentrated in the surface and

bottom mixed layers (Fig. 2). A detailed geography and analysis of turbulence, including the role of evolving shear, stratification, and Richardson number, is presented in MG05. They find that dissipation in the stratified mid water column is correlated with wave shear and is dependent on the gradient Richardson number.

## 4. Wave forcing: Energetics

In the next two sections, we seek to understand the evolving wave amplitude and vertical structure in terms of local forcing. In this section, we compare the evolution of depth-integrated wave energy with estimates of power gain or loss from the surface wind stress, bottom drag, and midcolumn turbulent dissipation. All are found to be of first-order importance. In section 5, we return to the modal decomposition and show how surface wind stress, bottom drag, and evolving stratification conspire to change the relative amplitudes of the first few modes. In all calculations below, we will use the variable  $E$  to refer to depth-averaged baroclinic kinetic energy; for convenience we refer to this quantity simply as energy.

### a. Surface wind stress

Slab mixed layer models have been widely and successfully used to explain the generation of near-inertial oscillations in the surface mixed layer by wind stress (Pollard and Millard 1970; Gill 1984; D’Asaro 1985; Zervakis and Levine 1995; Alford 2001). Such models assume that horizontal momentum imparted by the wind is quickly and evenly distributed vertically within

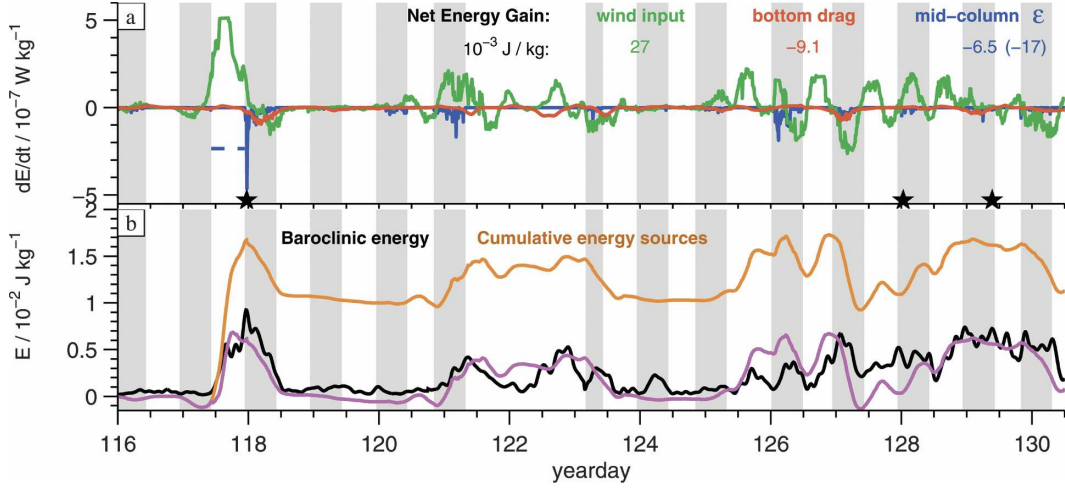


FIG. 7. (a) Estimated energy change from surface wind stress (green), bottom drag (red), and midcolumn dissipation (blue). Dissipation data were only available during MMP profiling times (shaded). Estimated average dissipation rate during yearday 117.5–118 (20) shown by a dotted blue line. The total measured energy input from each source is printed; average energy loss from turbulent dissipation including the estimate (20) is given in parentheses. (b) Observed baroclinic kinetic energy (black), the sum of cumulative energy change from all three processes (orange), and the cumulative energy change, including the estimated dissipation rate (20) (magenta). Velocity data have been supplemented with UCSB mooring data. The three black stars indicate the times of the profiles shown in Fig. 5.

the mixed layer and has no horizontal gradients. Mathematically, this is equivalent to forcing the momentum equations with a stress profile that is linear within the mixed layer (constant vertical derivative) and zero below. The evolution of mixed layer horizontal velocities is then given by

$$\begin{aligned} \frac{\partial u(t)}{\partial t} &= fv(t) + \frac{\tau_{sx}}{\rho_0 h_{ml}} - ru(t) \quad \text{and} \\ \frac{\partial v(t)}{\partial t} &= -fu(t) + \frac{\tau_{sy}}{\rho_0 h_{ml}} - rv(t), \end{aligned} \quad (6)$$

where  $\boldsymbol{\tau}_s = (\tau_{sx}, \tau_{sy})$  the surface wind stress,  $r$  is a damping coefficient that represents energy loss to unresolved processes (D'Asaro 1985), and  $\rho_0 = 1025 \text{ kg m}^{-3}$ . This conceptual model can be extended to consider the depth-dependent momentum equations, with a slablike forcing localized to the mixed layer. Eastward velocity, for example, would then evolve according to

$$\frac{\partial u(z, t)}{\partial t} = fv(z, t) + T_{sx}(z, t) - ru(z, t), \quad (7)$$

$$\begin{aligned} \mathbf{T}_s(z) &= \frac{1}{\rho_0} \frac{d\boldsymbol{\tau}}{dz} = \frac{\boldsymbol{\tau}_s}{\rho_0 h_{ml}}, \quad z \geq -h_{ml} \\ &= 0, \quad z < -h_{ml}, \end{aligned} \quad (8)$$

where  $h_{ml}$  is here defined to be 3 m below the bottom of the well-mixed surface layer (to account for the ac-

tive entrainment zone observed in MG05). For convenience, we have introduced a wind stress forcing function  $\mathbf{T}_s = (T_{sx}, T_{sy})$ , with units of acceleration. Energy input into baroclinic motions can be separately considered from the depth-averaged component; the baroclinic wind stress force ( $\text{m s}^{-2}$ ) is defined as

$$\mathbf{T}_{s\_bc}(z) = \mathbf{T}_s(z) - \frac{1}{H} \int_{-H}^0 \mathbf{T}_s(z) dz. \quad (9)$$

Baroclinic energy input (power) from surface wind stress is given by the depth-averaged dot product of baroclinic velocity and the wind stress forcing,

$$\left( \frac{dE}{dt} \right)_s = \frac{1}{H} \int_{-H}^0 [\mathbf{u}_{bc}(z, t) \cdot \mathbf{T}_{s\_bc}(z, t)] dz. \quad (10)$$

The average baroclinic power gain from wind stress was  $2.1 \times 10^{-8} \text{ W kg}^{-1}$ , though wind stress was alternately a source and sink of energy (Fig. 7). Integrated over a fortnight, the wind supplied  $27 \times 10^{-3} \text{ J kg}^{-1}$  of energy (Fig. 7, upper text). Previous work has shown that the most efficient energy fluxes occur when wind changes direction or magnitude over a time scale close to the inertial period and is in phase with existing inertial currents (Pollard and Millard 1970; Gill 1982; D'Asaro 1985). Consider the relationships between wind stress,

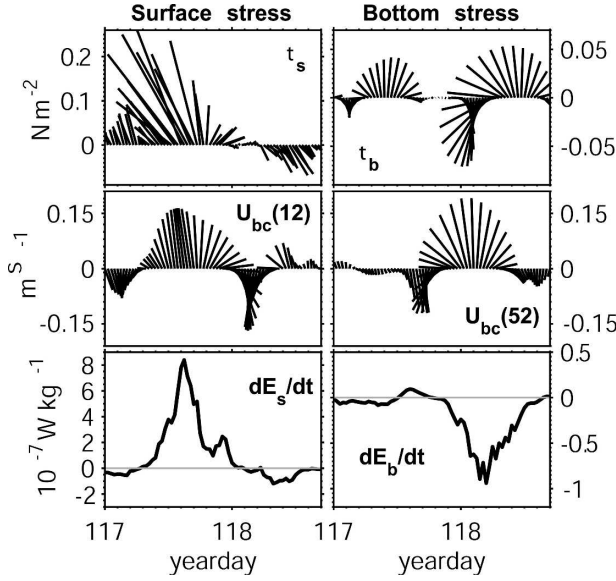


FIG. 8. (left) Surface and (right) bottom processes: (top) surface (bottom) stress, (middle) baroclinic velocity at 12 (52) m, and (bottom) depth-integrated power from each source (see text).

near-surface current, and wind power input during the first storm (Fig. 8, left). The strongest energy flux from the wind occurred when wind stress and near-surface currents were both strong, in the same direction, and rotating in a similar sense.

### b. Bottom drag

A major difference between wind forcing of near-inertial waves on the shelf and the open ocean is the relative proximity of the bottom and, thus, the possible role of bottom drag. Gill (1984) briefly considers the potential influence of bottom drag on near-inertial waves. He concludes that the decay rate from bottom drag is roughly proportional to the ratio of the bottom mixed layer to the total water depth, which for the open ocean is negligible. On the coast, however, the bottom mixed layer represents a significant percentage of the water column (Fig. 2). The magnitude ( $\text{J m}^{-2}$ ) and direction of bottom drag can be written as a function of the deepest measured *total* (baroclinic plus barotropic) velocity,

$$\begin{aligned}\tau_b &= -\rho_0 C_D |U_{bc} + U_{bt}| (\mathbf{U}_{bc} + \mathbf{U}_{bt}) \\ &= -\rho_0 C_D |U_{tot}| \mathbf{U}_{tot}.\end{aligned}\quad (11)$$

The drag coefficient ( $C_D$ ) represents the coupling between velocity variance at a particular depth (52 m in our case) and the drag felt by fluid near the seafloor. Dewey and Crawford (1988) relate the later to a turbulent dissipation rate within a constant stress layer close to the bottom. Shaw (2001) argue that the con-

stant stress assumption is valid only within a few meters of the bottom, a small subset of the full boundary layer. In this near-bottom layer, turbulence ( $\text{W kg}^{-1}$ ) and stress ( $\text{J m}^{-2}$ ) magnitude can be described by law-of-the-wall scalings (Dewey and Crawford 1988)

$$\varepsilon = \frac{u_*^3}{kz} \quad \text{and} \quad (12)$$

$$\tau_b = |\tau_b| = -\rho_0 u_*^2 = -C_D \rho_0 |U_{52}|^2. \quad (13)$$

The drag coefficient can thus be estimated by comparing measurements of (total) velocity at a reference level (52 m) and turbulent dissipation rate within a few meters of the bottom,

$$C_D = \frac{(kz_{\text{mab}}\varepsilon)^{2/3}}{|U_{52}|^2}, \quad (14)$$

where  $k$  is von Kármán's coefficient (0.4), and  $z_{\text{mab}}$  is the distance above bottom. Figure 9 plots the numerator versus the denominator of (14), based on microstructure measurements taken unintentionally close ( $\leq 2$  m) to the bottom. The best-fit line gives  $C_D = 10^{-3}$ .

The bottom stress calculated from (13) had an average magnitude of  $4.3 \times 10^{-2} \text{ N m}^{-2}$ , one-half that of surface stress (Fig. 2). The law-of-the-wall scaling (12) governs only the small region within a few meters of the bottom. Above this, we assume that momentum deficits are quickly distributed within the remainder of the bottom mixed layer. As with surface stress models, this assumption translates into a linear variation of stress ( $\text{m s}^{-2}$ ) with height,

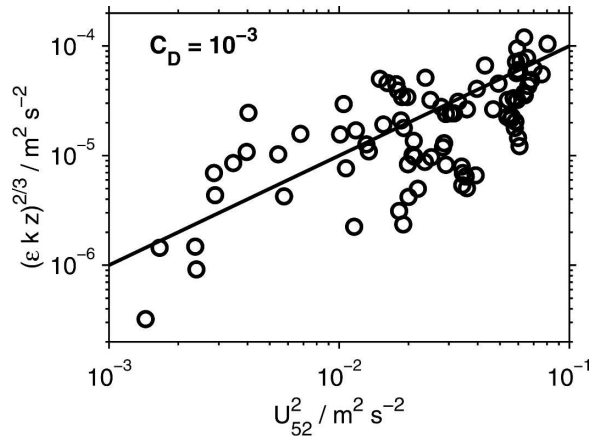


FIG. 9. Relationship between observed velocity at 52 m and turbulent velocity scale based on measured near-bottom turbulent dissipation rates (14). The slope of the least squares fit line ( $10^{-3}$ ) gives the estimated drag coefficient  $C_D$ .

$$\begin{aligned} \mathbf{T}_b(z) &= \frac{\tau_b}{\rho_0 h_{\text{bb1}}}, & z \leq -H + h_{\text{bb1}} \\ &= 0, & z > -H + h_{\text{bb1}} \end{aligned} \quad (15)$$

and

$$\mathbf{T}_{\text{b-bc}}(z) = \mathbf{T}_b(z) - \frac{1}{H} \int_{-H}^0 \mathbf{T}_b(z) dz. \quad (16)$$

Baroclinic power loss ( $\text{W kg}^{-1}$ ) from bottom-drag is given by the dot product of bottom stress forcing and baroclinic velocity,

$$\left( \frac{dE}{dt} \right)_b = \frac{1}{H} \int_{-H}^0 [\mathbf{u}_{\text{bc}}(z, t) \cdot \mathbf{T}_{\text{b-bc}}(z, t)] dz. \quad (17)$$

This rate can be evaluated by plugging (11) and (16) into (17) and noting that the integral is only nonzero for  $z \leq -H + h_{\text{bb1}}$ . Not surprisingly, bottom drag was a net baroclinic power drain, with an average magnitude of  $-7.3 \times 10^{-9} \text{ W kg}^{-1}$ , resulting in a net baroclinic energy loss of  $-9.1 \times 10^{-3} \text{ J kg}^{-1}$  (Fig. 7).

The barotropic tide played an important role in mediating baroclinic power loss from bottom drag. Combining (11) and (15)–(17), the magnitude of power loss from bottom drag roughly scales as

$$\left| \frac{dE}{dt} \right|_b \approx \frac{C_d}{H} |U_{\text{tot}}(52)|^2 |U_{\text{bc}}(52)| \cos\theta, \quad (18)$$

where  $\theta$  is the angle between the baroclinic and total velocity at 52 m (or equivalently the angle between baroclinic velocity and bottom stress), from the dot product in (17). The vast majority of bottom stress variance (87%) was due to the barotropic component of velocity. However, substituting  $\mathbf{U}_{\text{tot}} \approx \mathbf{U}_{\text{bt}}$  in (11) yields only 3% of the actual power loss! The key is the third term in (18);  $\cos(\theta)$  is correlated with  $|U_{\text{bc}}| |U_{\text{tot}}|^2$  (correlation coefficient of 0.34), but not with  $|U_{\text{bc}}| |U_{\text{bt}}|^2$  (correlation coefficient of 0.08). Conceptually, the average phase ( $\theta$ ) between barotropic (tidal) and baroclinic (near inertia) currents is close to 0. On the other hand, substituting  $\mathbf{U}_{\text{bc}}$  for  $\mathbf{U}_{\text{tot}}$  replicates 42% of the total power loss. The strongest energy losses occur when the baroclinic and barotropic velocities are in phase. For example, the large energy loss from bottom stress on yearday 118 took place when total (top) and baroclinic (middle) currents were both large (Fig. 7, right).

### c. Turbulent dissipation

Stratified turbulent energy dissipation may also drain energy from the baroclinic flow. Turbulent dissipation

within the surface and bottom mixed layers is already accounted for in our expressions for energy gain/loss from surface/bottom drag. The remaining depth-averaged baroclinic energy loss from turbulent dissipation is estimated as the sum of measured dissipation in the stratified water between surface and bottom mixed layers,

$$\left( \frac{dE}{dt} \right)_{\text{interior}} = \frac{1}{H} \int_{Z_{\text{bb1}}}^{Z_{\text{sml}}} \varepsilon(z) dz. \quad (19)$$

The average power loss from measured turbulent dissipation was  $-1.2 \times 10^{-8} \text{ W kg}^{-1}$ , resulting in a net energy loss of  $-6.5 \times 10^{-3} \text{ J kg}^{-1}$  (Fig. 7). Note that dissipation measurements were only available during MMP profiling periods (shaded).

Unfortunately, the strongest turbulence may have occurred during the height of the first storm (yeardays 117.5–118) when no microstructure measurements were made. The average dissipation rate during this period can be estimated by considering the depth-averaged potential energy change,

$$\varepsilon_{\text{estimated}} \sim \frac{\text{PE}_f - \text{PE}_i}{\gamma \rho \Delta t} \quad \text{and} \quad (20)$$

$$\text{PE}_{f,i} \equiv \frac{1}{H} \int_{-H}^0 \rho_{f,i} g z dz, \quad (21)$$

where  $\text{PE}_{f,i}$  and  $\rho_{f,i}$  are the final (yearday 118) and initial (yearday 117.5) potential energy and density of the water column,  $\Delta t$  is the time over which mixing is assumed to occur (0.5 days), and  $\gamma$  is a mixing efficiency (0.2). The average dissipation rate calculated from (20) is  $2.35 \times 10^{-7} \text{ W kg}^{-1}$ , which brings the cruise average to  $2.8 \times 10^{-8} \text{ W kg}^{-1}$ . Including the estimated dissipation from (20), the integrated energy loss to turbulence over the fortnight was  $17 \times 10^{-3} \text{ J kg}^{-1}$  (Fig. 7).

### d. Energetics comparisons and time scales

Surface wind stress, bottom drag, and interior dissipation were all, at times, of comparable magnitude (Fig. 7a). The total integrated energy input/loss from each of the three terms nearly balance, especially when the estimated average dissipation during the first storm is included. The observed energy changes can be compared with integrated estimates of energy input from wind stress (10), bottom stress (17), and midcolumn turbulent dissipation (19). Cumulative modeled energy (orange) shares many features with the actual baro-

TABLE 1. Characteristic time scales (22) associated with baroclinic power sources and sinks, and wave propagation (23), in days. Negative values indicate a process that is a net power sink.

	Surface stress	Bottom stress	Midcolumn dissipation	Mode-1 propagation	Mode-2 propagation
Mean	1.2	-2	-1.7	22.7	52.1
Yearday 118	1.1	-1.5	-1.3	35.7	100
Yearday 128	0.45	-4.6	-11.6	17.2	38.5
Yearday 29.4	16.7	-38.5	-6.8	16.1	35.7

clinic energy evolution, but diverges substantially during the first storm (Fig. 7b). When the estimated average dissipation rate during the storm (20) is included, the modeled cumulative energy (magenta) stays much more closely aligned with the observed energy changes.

All three power sources were strong enough, on average, to change wave energy significantly over approximately one day. Table 1 shows characteristic time scales ( $t$ ) of energy growth and decay for each process based upon

$$t = \frac{E_{bc}}{|dE/dt|} = \frac{1}{2r}. \quad (22)$$

Here  $r$  is a decay rate, dimensionally consistent with (6) and (28). The three sample periods listed are those shown in Fig. 5. For reference, we also show time scales of estimated energy change from wave propagation,

$$t_{prop} = \frac{L}{c_g}, \quad (23)$$

based upon the group velocity ( $c_g$ ) of first- and second-mode waves of frequency  $1.05f$  (a function of evolving stratification) and a characteristic length scale  $L$  of 50 km (the distance to the nearest natural boundary, the shelf break). These characteristic time scales of local energy sources and sinks are conceptually consistent with quick energy input by surface wind stress (under one day), and only slightly slower energy loss through bottom drag and turbulent dissipation (under two days). Since all three time scales are significantly shorter than characteristic propagation times for the first two modes, we conclude that wave energetics were generally consistent with local generation and decay.

During the early period (yearday 118), the three local energy sources/sinks are all of equivalent importance. There is a substantial decrease in the strength of turbulent energy loss (a growing time scale) between year-days 118 and 128. MG05 links this change to a regime shift in the controlling mechanism of turbulence, from

instability of the lowest modes to finescale wave-wave interactions. By the end of the fortnight the time scales for local forcing or wave decay have grown comparable to or larger than propagation time scales. Shearman (2005) points out that the propagation speed of *barotropic* waves is, however, significantly faster than that of baroclinic modes, and a barotropic response reflected off the coastline may also play a role in determining inertial currents offshore.

## 5. Wave forcing: Vertical structure

In this section, the evolving vertical wave structure is related to the changing mode shape and the differential coupling of surface and bottom stresses into baroclinic modes. Following Gill (1984), the momentum added to the surface mixed layer through wind stress can be projected onto vertical mode shapes (1). The power input into each mode ( $\text{W kg}^{-1}$ ) can be calculated by plugging (3) into (10) (Gill 1984),

$$\left(\frac{dE}{dt}\right)_{s,j} = \frac{1}{H} \int_{-H}^0 [\mathbf{U}_j(t) \cdot \mathbf{T}_{s-bc}(z, t)] \frac{\partial \psi_j(z)}{\partial z} dz. \quad (24)$$

A similar procedure yields the power lost from each mode ( $\text{W kg}^{-1}$ ) due to bottom drag,

$$\left(\frac{dE}{dt}\right)_{b,j} = \frac{1}{H} \int_{-H}^0 [\mathbf{U}_j(t) \cdot \mathbf{T}_{b-bc}(z, t)] \frac{\partial \psi_j(z)}{\partial z} dz, \quad (25)$$

where the magnitude of bottom drag ( $\mathbf{T}_b$ ) is controlled by the sum of velocity from all modes, as well as from the barotropic tide (11).

Power sources and sinks from surface (24) and bottom (25) forcing are calculated for the first two baroclinic modes using 10-min averages of velocity. Mixed layer depths and wind stress measurements are interpolated onto these times. It is not obvious how midcolumn turbulent dissipation (19) differentially drains energy from distinct baroclinic modes; it is hence not ex-

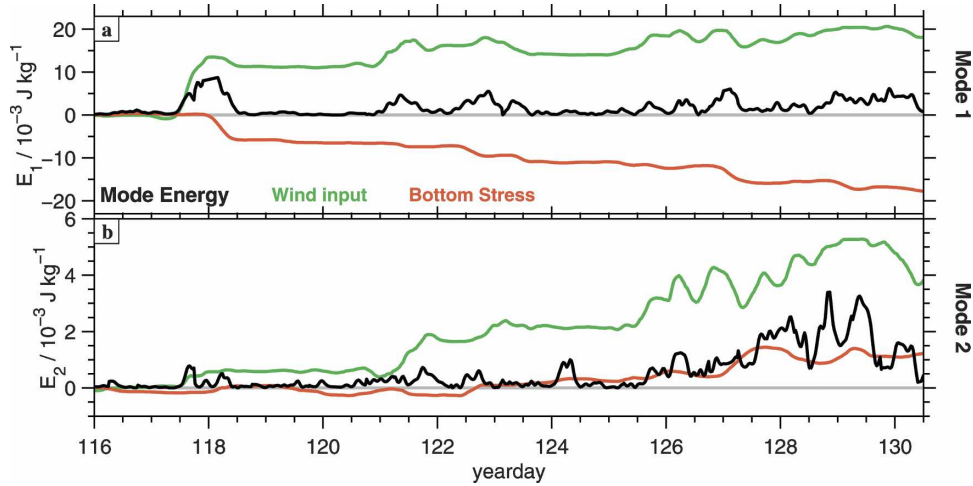


FIG. 10. (a) Energy of first baroclinic mode (black) and estimated cumulative energy input from surface stress (green) and bottom stress (red) projected onto the vertical mode shape. (b) As in (a), but for second baroclinic mode.

plicitly considered in modal energy budgets, though it is clearly a drain on total wave energy (Fig. 7).

#### a. Modal energy input: Wind stress

Wind stress forcing (24) provided an average power input into the first and second modes of  $1.5 \times 10^{-8}$  and  $2 \times 10^{-9} \text{ W kg}^{-1}$ , respectively (Fig. 10, green). The stronger power going into the first mode reflects both the larger-mode energy (Fig. 6) and the stronger projection of wind stress onto mode 1 ( $0.1 \text{ N m}^{-2}$ , on average), relative to mode 2 ( $0.05 \text{ N m}^{-2}$ ). This difference in projected wind stress is due to the relatively larger mode-1 surface expression (Fig. 5).

The proportion of wind stress projected onto mode 2 doubled over the fortnight as the mixed layer shoaled. During the first storm (yearday 118), strong turbulence set  $h_{\text{ml}} \approx 25 \text{ m}$ ; wind stress projected onto the second mode over this period was only 30% of the mode-1 wind stress projection. For a brief period near yearday 117.5, wind stress actually drained power from mode 2 as modal velocity and wind stress were out of phase. However, this period coincided with rapid stratification changes due to mixed layer deepening, and estimated mode-2 amplitude and phase are suspect. After yearday 125, the efficiency of wind stress coupling into the second mode rose to 60% of mode-1 wind stress.

#### b. Modal energy input: Bottom stress

On average, bottom stress (25) drained energy from the first mode ( $-1.5 \times 10^{-8} \text{ W kg}^{-1}$ ) but added energy to the second mode ( $1.1 \times 10^{-9} \text{ W kg}^{-1}$ ) (Fig. 10). This

surprising observation is one of the major results of this paper. The strongest gains of power from bottom drag for mode 2 occurred on yearday 127 (Figs. 7, 10). At this time, the mode-1 near-bottom velocity and the barotropic tide were both strong and in phase, and the quadratic nature of bottom drag allowed efficient removal of energy from mode-1 waves. Mode-1 and mode-2 waves were in phase at the surface (correlation coefficient of 0.76), which implies  $\mathbf{U}_1 \sim \mathbf{U}_2$  (24). As a result, first- and second-mode velocities were of opposite sign at depth (Fig. 5):

$$\frac{\partial \psi_1(z)}{\partial z} \sim -\frac{\partial \psi_2(z)}{\partial z} - H < z < -H + h_{\text{bbl}}.$$

Therefore, power changes in the first and second modes due to bottom stress [(25)] were opposite in sign. As the stratification changed from yearday 118 to 126, the relative amplitude of the mode-2 bottom expression rose from one-half of the magnitude of mode 1 to nearly equal (Fig. 5), allowing a more efficient transfer of energy.

Our conclusion is that the rising relative importance of mode-2 waves after yearday 126 (section 3d) is due to both an increased efficiency of wind energy modal transfer and a growing nonlinear energy transfer between first- and second-mode waves through quadratic bottom drag.

## 6. Extended mixed layer model

The observations and analysis in the preceding several sections suggest that the evolving magnitude and

vertical structure of near-inertial internal waves were consistent with local forcing by wind stress, bottom drag, and midcolumn turbulent dissipation. In this section, we incorporate those mechanisms into a simple numerical model of wave generation. Comparison of model results with data allows us to test the hypotheses of surface and bottom wave forcing formed in the previous sections and explore how sensitive resultant waves are to variations in forcing parameters.

### a. Model description

The model is based on the slab mixed-layer-type models used in the open ocean (Pollard and Millard 1970; D'Asaro 1995; Alford 2001). Here a similar mixed layer model is extended to two dimensions by projecting wind stress onto prescribed mode shapes and incorporating a tidally mediated bottom drag. Horizontal velocity ( $\text{m s}^{-1}$ ) is written as a sum of baroclinic modes with prescribed horizontal wavenumber [cf. (3)],

$$u(x, y, z, t) = \sum_j U_j(t) e^{ily} \frac{\partial \psi_j}{\partial z} \quad \text{and} \quad (26)$$

$$v(x, y, z, t) = \sum_j V_j(t) e^{ily} \frac{\partial \psi_j}{\partial z}. \quad (27)$$

The horizontal wavenumber  $l$  is a free parameter; for simplicity we choose a northward wave vector with a characteristic length scale set by the distance to the coast  $l = 2\pi/100 \text{ km}$  for all vertical modes. Sensitivity to this choice is discussed in section 6c.

At each time step, modal projections of surface and bottom stress derivatives are applied as body forces within surface and bottom mixed layers. Wind stress forcing ( $\mathbf{T}_s$ ) is projected onto each vertical mode. The (vector) amplitude of each mode is then rotated forward in time, consistent with the dispersion relationship for a given mode number and wave vector (Gill 1982),

$$\frac{dU_j}{dt} = fV_j + T_{sx}(j) + T_{bx}(j) - rU_j, \quad (28)$$

$$\frac{dV_j}{dt} = -f \left( 1 + \frac{l^2}{f^2} c_j^2 \right) U_j + T_{sy}(j) + T_{by}(j) - rV_j, \quad (29)$$

$$\mathbf{T}_s(j) = \frac{1}{H} \int_{-H}^0 \mathbf{T}_{s\text{-bc}}(z, t) \frac{\partial \psi_j(z)}{\partial z} dz, \quad \text{and} \quad (30)$$

$$\mathbf{T}_b(j) = \frac{1}{H} \int_{-H}^0 \mathbf{T}_{b\text{-bc}}(z, t) \frac{\partial \psi_j(z)}{\partial z} dz, \quad (31)$$

where  $c_j$  is the separation constant from (1), which we will also refer to as mode speed. Note that the horizontal pressure gradients neglected in (7) are now implicitly included through the prescribed horizontal wavenumber  $l$ . Surface stress forcing ( $\mathbf{T}_s$ ) is calculated from the observed wind stress (9), and bottom stress is calculated at each time step based on the sum of modeled baroclinic velocity plus and the observed barotropic tide [(11)–(16)]. Energy is removed using a linear Rayleigh drag term to account for unresolved energy losses, primarily turbulent dissipation. We choose  $r = 0.29 \text{ day}^{-1}$  to match the average decay rate from midcolumn dissipation (Table 1). The wisdom of using a uniform decay rate at all times is discussed below.

### b. Model results

The model consists of frictionless freely propagating waves that cannot be expected to match every feature of the data. Nevertheless, the model successfully reproduces the basic amplitude response and changing vertical structure of observed waves (Fig. 11). Similar features between modeled and observed waves include strong mode-1 waves on yearday 118 following the first storm, weaker higher modes on yeardays 121–123 (a surprising agreement given the uncertainties in calculated mode shapes owing to lack of stratification data during this period), and the emergence of a larger mode-2 wave component after yearday 126. The amplitude and phase of observed and modeled velocity can be more clearly seen in Fig. 12. The model velocity is in phase with observed velocity during yearday 118 and after yearday 126; the correlation coefficient between observed and modeled northward velocity at 12 m is 0.87 during these two periods and 0.77 overall.

The model successfully reproduces the rising strength of mode-2 waves and the importance of bottom drag as a mode-2 energy source (cf. Figs. 13 and 10). Surface wind stress is a source of power for both mode-1 ( $1.1 \times 10^{-8} \text{ W kg}^{-1}$ ) and mode-2 waves ( $7.5 \times 10^{-10} \text{ W kg}^{-1}$ ). Bottom stress is a net sink of power for the first mode ( $-5.9 \times 10^{-9} \text{ W kg}^{-1}$ ), and a net source of power for the second mode ( $1.2 \times 10^{-9} \text{ W kg}^{-1}$ ).

### c. Model sensitivity

#### 1) RAYLEIGH DECAY RATE

The accuracy of modeled wave energy suffers from the substitution of a simplistic Rayleigh drag for turbulent energy losses. Modeled waves after yearday 118 persist for several periods after observed waves die away, while modeled waves after 126 are excessively damped (Fig. 12). Analysis in section 4 showed that the

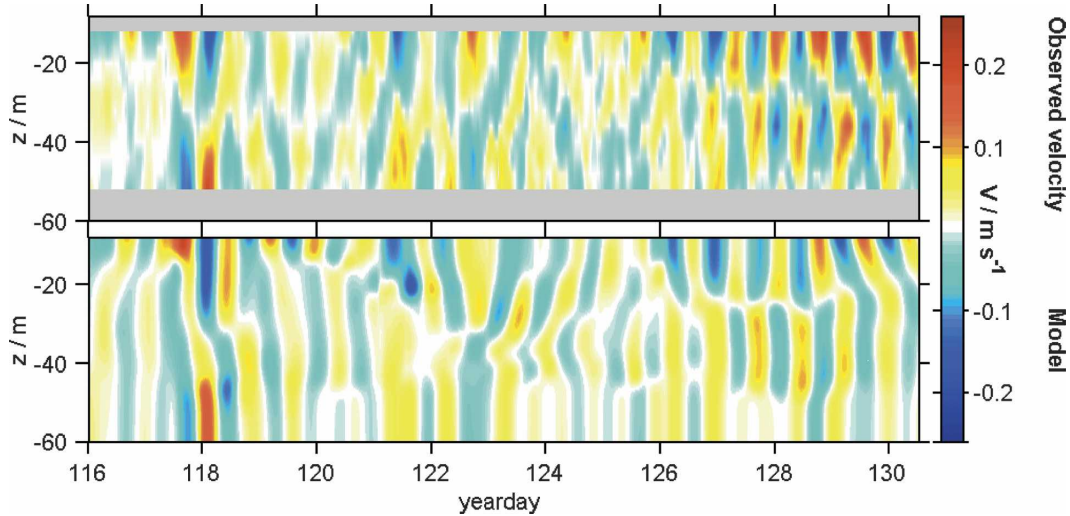


FIG. 11. (top) Northward baroclinic velocity (data during yeardays 121–123 from UCSB mooring). (bottom) Model northward baroclinic velocity.

magnitude and associated time scale of turbulent energy loss changed significantly over the fortnight, an effect not accounted for by the use of a single Rayleigh drag coefficient for all times (Fig. 7, Table 1).

Changing the modeled Rayleigh decay rate  $r$  qualitatively alters the modal energetic balances and the rate of energy transfer between modes. Doubling the decay rate (halving the characteristic time scale) decreases the mode-1, mode-2, and total (all modes) average baroclinic energies by 25%, 30%, and 54%, respectively. On the other hand, halving the decay rate increases total average baroclinic energy by 25%, but increases mode-1 energy by only 4% on average: increases in mode-1 energy from lower frictional losses are compensated for by a stronger loss to bottom drag. Stronger bottom drag in turn transfers more energy to mode-2 waves, resulting in a 61% increase in average mode-2 energy. The primary mode-2 energy balance is then

between gain from bottom drag and loss from Rayleigh friction, with direct wind stress power playing a minor role.

## 2) BOUNDARY LAYER DEPTH

Varying the depth ranges ( $h_{ml}$ ,  $h_{bbi}$ ) over which body forces are applied had a progressively larger effect on higher modes. Recall that in the model wind stress is applied from the surface to 3 m below the depth of the well-mixed surface layer to account for active entrainment ( $h_{ml}$ ); decreasing (increasing) the lower boundary of this range to 0 m (5 m) below the depth of the well-mixed layer changes the wind power going into the first mode by 10% (–10%), and the power going into the second mode by 60% (–12%). The stronger mode-2 response to a smaller  $h_{ml}$  is due to the rapid decrease in integrated mode-2 amplitude with depth below the surface mixed layer (e.g., Fig. 5). The net transfer of

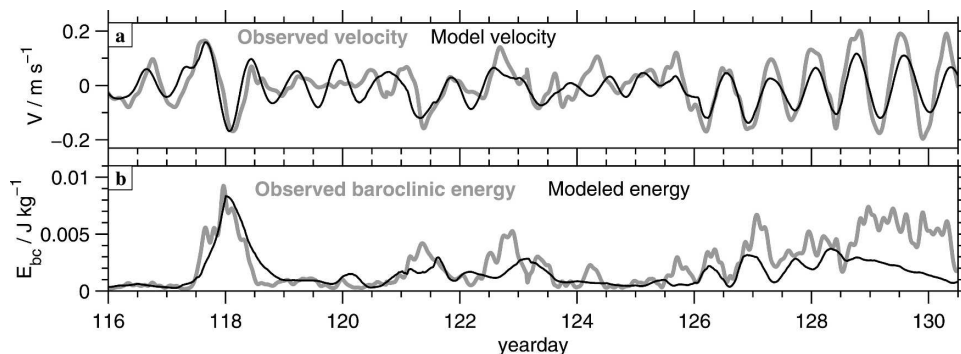


FIG. 12. (a) Observed (thick, gray) and modeled (thin, black) baroclinic velocity at 12 m. (b) Observed and modeled baroclinic energy averaged between 12 and 52 m, the depth range of ADCP measurements.

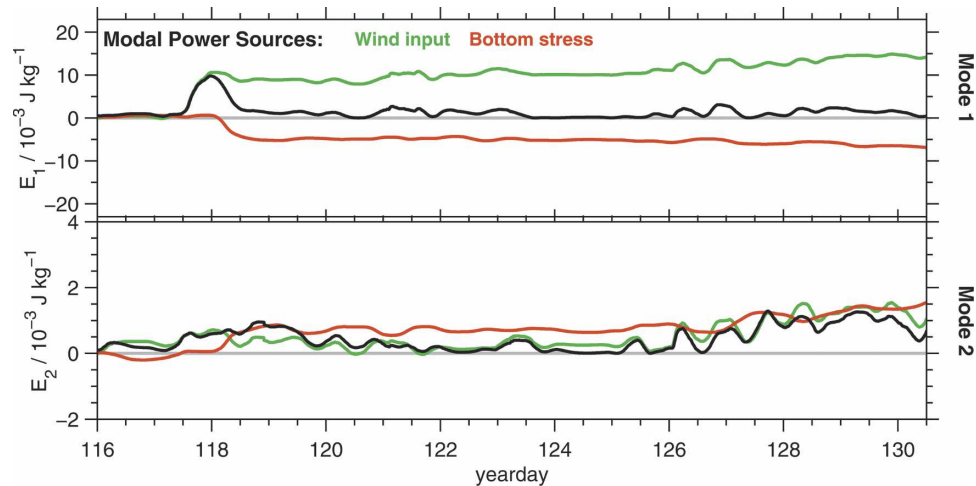


FIG. 13. (top) Modeled energy in the first baroclinic mode (black), and cumulative modal energy change from wind stress (green) and bottom drag (red). (bottom) As in (top), but for second baroclinic mode. The axes limits are the same as in Fig. 10.

energy between first- and second-mode waves depends on the application of bottom stress over a thick bottom layer ( $h_{bb}$ ); halving this depth changed the bottom stress into a net sink of power for mode-2 waves ( $-5.5 \times 10^{-10} \text{ W kg}^{-1}$ ).

### 3) BAROTROPIC TIDE

As demonstrated with observational data analysis in section 4b, the coupling of the barotropic tide with baroclinic currents significantly increases the strength of bottom drag. If the modeled bottom drag is based upon baroclinic currents alone, the mode-1 power loss to bottom drag drops by 60%, raising the average mode-1 energy by 25% (the difference is taken up by a larger Rayleigh stress loss). Bottom drag is still a net source of power to mode-2 waves, but is reduced by 70%.

### 4) HORIZONTAL WAVE SCALES

The model assumes that a simple horizontal wavelength characterizes not only the waves but, implicitly, also the forcing terms. In general, baroclinic modes have smaller horizontal scales than the barotropic tide. As a result, half a (baroclinic) wavelength away the nonlinear transfer of energy between the barotropic tide and baroclinic wave through bottom drag will be of opposite sign at any given point in time.

However, the model is relatively insensitive to changes in the magnitude or direction of the horizontal wavenumber  $l$ . The modeled wavelength was chosen to match the distance to the coast ( $\sim 100 \text{ km}$ ); another reasonable choice is the distance to the shelfbreak front

( $\sim 40 \text{ km}$ ; Barth et al. 1998). Doubling the magnitude of  $l$  slightly increases the frequency of generated waves. For early waves that do not last for more than an inertial period or two, the increase in frequency has little effect. However, for the waves appearing after yearday 126, the change in frequency results in a growing difference between wind and wave phase relationships; the net effect is a 7% increase in energy input from the wind. Halving the magnitude of  $l$  has less than a 2% effect on all energetics. Rotating the wavenumber direction from northward to eastward results in less than a 1% change in all energetics; near-inertial waves are close to circular and slight changes in ellipticity do not alter the efficiency of wind-wave energy transfer.

## 7. Conclusions

Strong low-mode, near-inertial internal waves were observed on the shelf in the spring, with variable magnitude and vertical structure. The major goal of this paper is to investigate the evolution of internal waves during this period of rapidly changing stratification. In particular, we are interested in understanding the magnitude and location of wave shear, which is used to diagnose and parameterize turbulent mixing in MG05. Our major conclusions are as follows:

- Internal waves were created by the wind stress of passing storms. During the first week (characteristic of early spring), the generated waves had a first-mode vertical structure. Moderate shear and weak stratification led to subcritical Richardson numbers and energetic turbulence that drained the wave energy over

the course of one wave period. As the stratification strengthened and storms weakened (characteristic of late spring), the Richardson numbers of near-inertial waves rose, allowing waves to persist for many periods, well after the end of surface forcing.

- Changes in vertical wave structure reflected both the changing shapes of baroclinic vertical modes (as stratification changed) and the changing relative strength of each mode. Over the fortnight, there was a systematic increase in the relative strength of mode-2 waves. This shift was due to two comparably sized factors. First, an increasing percentage of wind stress was projected onto (forced) mode-2 waves as the stratification grew and the surface mixed layer (over which wind stress was applied) shoaled. Second, quadratic bottom drag transferred energy from mode-1 to mode-2 waves. The impact of bottom drag was largest when the near-bottom expressions of low-mode baroclinic waves were in phase with the barotropic tide. The first-order importance of bottom drag is in stark contrast to the near-inertial wave generation in the open ocean.

A two-dimensional slab mixed layer model is proposed that projects wind stress forcing onto observed vertical mode shapes and includes a bottom-drag term incorporating the observed barotropic tide. The model roughly reproduces the correct magnitude and phase of observed near-inertial waves. The model also successfully captures the rising strength of mode-2 waves and confirms the transfer of energy between mode-1 and mode-2 waves through bottom drag. Model results suggest two dynamical veins for further exploration:

- 1) The model was most sensitive to changes in the depth range over which surface and bottom stresses were applied, in particular to the assumed depth of a turbulent entrainment layer at the boundary edge. Higher-resolution velocity measurements in similar environments could help clarify the depth range over which surface momentum additions are mixed.
- 2) The largest problem with the model is the use of a simple Rayleigh drag to parameterize loss to turbulent dissipation, which drains energy at a rate linearly proportional to the wave energy. However, in MG05 we show that the functional relationship between dissipation rate and shear goes through a regime change as stratification strengthens. We conclude that a class of models similar to the one proposed here has good potential for understanding wave generation on the shelf, but will be limited until more realistic parameterizations of turbulent energy loss are included.

The value of such a model combining prognostic equations with assimilated data is in the credibility it brings to our dynamical hypotheses rather than its suitability for “off the shelf” use in the present form. Nevertheless, we hope our observations of the importance of changing modal distributions and the role of bottom drag will be helpful for future treatments of internal waves in shallow environments.

*Acknowledgments.* We thank Jody Klymak, Earl Krause, Jack Miller, Gordon Welsh, and the entire crew of the R/V *Knorr* for help with data collection. Numerous other CMO investigators generously shared their thoughts and results with us. We particularly thank Tommy Dickey for sharing mooring data, as well as Wilf Gardner, Murray Levine, Tim Boyd, and Jack Barth. We appreciate the detailed comments of two anonymous reviewers, which significantly helped to clarify the paper. This work was supported by ONR Grant N00014-95-1-0406. Author J. MacKinnon received additional support from an NDSEG research fellowship; M. Gregg received additional support from the SECNAV/CNO Chair in Oceanography.

#### REFERENCES

- Alford, M. H., 2001: Internal swell generation: The spatial distribution of energy flux from the wind to mixed layer near-inertial motions. *J. Phys. Oceanogr.*, **31**, 2359–2368.
- Apel, J., L. Ostrovsky, and Y. A. Stepanyants, 1995: Internal solitons in the ocean. Applied Physics Laboratory, The Johns Hopkins University, Tech. Rep. MERCJRA0695, 67 pp.
- Barth, J. A., D. Bogucki, S. D. Pierce, and P. M. Kosro, 1998: Secondary circulation associated with a shelfbreak front. *Geophys. Res. Lett.*, **25**, 2761–2764.
- Chant, R. J., 2001: Evolution of near-inertial waves during an upwelling event on the New Jersey inner shelf. *J. Phys. Oceanogr.*, **31**, 746–764.
- Chen, C., R. O. Reid, and W. D. Nowlin Jr., 1996: Near-inertial oscillations of the Texas-Louisiana shelf. *J. Geophys. Res.*, **101** (C2), 3509–3524.
- Colosi, J., R. C. Beardsley, J. Lynch, G. Gawarkiewicz, C.-S. Chiu, and A. Scotti, 2001: Observations of nonlinear internal waves on the outer New England continental shelf during summer shelfbreak primer. *J. Geophys. Res.*, **106** (C5), 9587–9602.
- D’Asaro, E., 1985: The energy flux from the wind to near-inertial motions in the mixed layer. *J. Phys. Oceanogr.*, **15**, 943–959.
- , 1995: A collection of papers on the ocean storms experiment. *J. Phys. Oceanogr.*, **25**, 2817–2818.
- , C. Eriksen, M. Levine, P. Niller, C. Paulson, and P. van Meurs, 1995: Upper-ocean inertial currents forced by a strong storm. Part 1: Data and comparisons with linear theory. *J. Phys. Oceanogr.*, **25**, 2909–2936.
- Dewey, R. K., and W. R. Crawford, 1988: Bottom stress estimates from vertical dissipation rate profiles on the continental shelf. *J. Phys. Oceanogr.*, **18**, 1167–1177.
- Fairall, C., E. Bradley, D. Rogers, J. Edson, and G. Young, 1996: Bulk parameterization of air–sea fluxes for tropical ocean

- global atmosphere coupled ocean atmosphere response experiment. *J. Geophys. Res.*, **101** (C2), 3747–3764.
- Gardner, W. D., and Coauthors, 2001: Optics, particles, stratification, and storms on the New England continental shelf. *J. Geophys. Res.*, **106**, 9473–9498.
- Gill, A., 1984: On the behavior of internal waves in the wakes of storms. *J. Phys. Oceanogr.*, **14**, 1129–1151.
- , 1982: *Atmosphere-Ocean Dynamics*. Academic, 662 pp.
- Gregg, M. C., 1989: Scaling turbulent dissipation in the thermocline. *J. Geophys. Res.*, **94** (C7), 9686–9698.
- Holloway, P. E., P. G. Chatwin, and P. Craig, 2001: Internal tide observations from the Australian North West shelf in summer 1995. *J. Phys. Oceanogr.*, **31**, 1182–1199.
- Kunze, E., A. J. Williams III, and M. G. Briscoe, 1990: Observations of shear and vertical stability from a neutrally buoyant float. *J. Geophys. Res.*, **95** (C10), 18 127–18 142.
- Lentz, S., K. Shearman, S. Anderson, A. Plueddemann, and J. Edson, 2003: Evolution of stratification over the New England shelf during the Coastal Mixing and Optics study, August 1996–June 1997. *J. Geophys. Res.*, **108**, 3008, doi:10.1029/2001JC001121.
- Levine, M. D., 2002: A modification of the Garrett–Munk internal wave spectrum. *J. Phys. Oceanogr.*, **32**, 3166–3181.
- MacKinnon, J., and M. Gregg, 2003a: Mixing on the late-summer New England shelf—Solibores, shear, and stratification. *J. Phys. Oceanogr.*, **33**, 1476–1492.
- , and —, 2003b: Shear and baroclinic energy flux on the summer New England shelf. *J. Phys. Oceanogr.*, **33**, 1462–1475.
- , and —, 2005: Spring mixing: Turbulence and internal waves during restratification on the New England shelf. *J. Phys. Oceanogr.*, **35**, 2425–2443.
- Miles, J., 1961: On the stability of heterogenous shear flows. *J. Fluid Mech.*, **10**, 496–512.
- Moehlis, J., and S. G. Llewellyn-Smith, 2001: Radiation of mixed layer near-inertial oscillations into the ocean interior. *J. Phys. Oceanogr.*, **31**, 1550–1560.
- Pollard, R., and R. Millard, 1970: Comparison between observed and simulated wind-generated inertial oscillations. *Deep-Sea Res.*, **17**, 153–175.
- Polzin, K., 1996: Statistics of the Richardson number: Mixing models and finestructure. *J. Phys. Oceanogr.*, **26**, 1409–1425.
- , J. M. Toole, and R. W. Schmitt, 1995: Finescale parameterizations of turbulent dissipation. *J. Phys. Oceanogr.*, **25**, 306–328.
- Rippeth, T. P. and M. E. Inall, 2002: Observations of the internal tide and associated mixing across the Malin shelf. *J. Geophys. Res.*, **107**, 3028, doi:10.1029/2000JC000761.
- Sandstrom, H., J. Elliott, and N. Cochrane, 1989: Observing groups of solitary internal waves and turbulence with batfish and echo-sounder. *J. Phys. Oceanogr.*, **19**, 987–997.
- Shaw, W., III, 2001: Budgets of turbulent kinetic energy and scalar variance in the continental shelf bottom boundary layer. *J. Geophys. Res.*, **106** (C5), 9551–9564.
- Shearman, R. K., 2005: Observations of near-inertial current variability on the New England shelf. *J. Geophys. Res.*, **110**, C02012, doi:10.1029/2004JC002341.
- Thorpe, S., 1978: On the shape and breaking of finite amplitude internal gravity waves in a shear flow. *J. Fluid Mech.*, **85**, 7–32.
- , 1998: Estimating internal waves and diapycnal mixing from conventional mooring data in a lake. *Limnol. Oceanogr.*, **43**, 936–945.
- van Haren, H., L. Mass, J. Zimmerman, H. Ridderinkhof, and H. Malschaert, 1999: Strong inertial currents and marginal internal wave stability in the central North Sea. *Geophys. Res. Lett.*, **26**, 2993–2996.
- Young, W., and M. Ben-Jelloul, 1997: Propagation of near-inertial oscillations through a geostrophic flow. *J. Mar. Res.*, **55**, 735–766.
- Zervakis, V., and M. Levine, 1995: Near-inertial energy propagation from the mixed layer: Theoretical considerations. *J. Phys. Oceanogr.*, **25**, 2872–2889.